

LETTER TO THE EDITOR

Discovery of HCCCO and C₅O in TMC-1 with the QUIJOTE¹ line survey[★]

J. Cernicharo¹, M. Agúndez¹, C. Cabezas¹, B. Tercero^{2,3}, N. Marcelino³, R. Fuentetaja¹ JR. Pardo¹, P. deVicente²¹ Grupo de Astrofísica Molecular, Instituto de Física Fundamental (IFF-CSIC), C/ Serrano 121, 28006 Madrid, Spain. e-mail: jose.cernicharo@csic.es² Centro de Desarrollos Tecnológicos, Observatorio de Yebes (IGN), 19141 Yebes, Guadalajara, Spain.³ Observatorio Astronómico Nacional (OAN, IGN), Madrid, Spain.

Received; accepted

ABSTRACT

We report on the detection, for the first time in space, of the radical HCCCO and of pentacarbon monoxide, C₅O. The derived column densities are $(1.6\pm 0.2)\times 10^{11}$ cm⁻² and $(1.5\pm 0.2)\times 10^{10}$ cm⁻², respectively. We have also analysed the data for all the molecular species of the families HC_nO and C_nO within our QUIJOTE¹'s line survey. Upper limits are obtained for HC₄O, HC₆O, C₄O, and C₆O. We report a robust detection of HC₅O and HC₇O based on 14 and 12 rotational lines detected with a signal-to-noise ratio ≥ 30 and ≥ 5 , respectively. The derived N(HC₃O)/N(HC₅O) abundance ratio is 0.09 ± 0.03 , while N(C₃O)/N(C₅O) is 80 ± 2 , and N(HC₅O)/N(HC₇O) is 2.2 ± 0.3 . As opposed to the cyanopolyne family, HC_{2n+1}N, which shows a continuous decrease in the abundances with increasing *n*, the C_nO and HC_nO species show a clear abundance maximum for *n*=3 and 5, respectively. They also show an odd and even abundance alternation, with odd values of *n* being the most abundant, which is reminiscent of the behaviour of C_nH radicals, where in that case species with even values of *n* are more abundant. We explored the formation of these species through two mechanisms previously proposed, which are based on radiative associations between C_nH_m⁺ ions with CO and reactions of C_n⁻ and C_nH⁻ anions with O atoms, and we found that several species, such as C₅O, HC₄O, and HC₆O, are significantly overestimated. Our understanding of how these species are formed is incomplete as of yet. Other routes based on neutral-neutral reactions such as those of C_n and C_nH carbon chains with O, OH, or HCO, could be behind the formation of these species.

Key words. molecular data — line: identification — ISM: molecules — ISM: individual (TMC-1) — astrochemistry

1. Introduction

Recent observations of the molecular cloud TMC-1 with the Yebes 40m (Cernicharo et al., 2021a) and Green Bank (McGuire et al., 2018) radio telescopes have shown that this source presents a paramount challenge to our understanding of the chemical processes in cold prestellar cores. The detection of cyclopentadiene and indene (Cernicharo et al., 2021b), ortho-benzene (Cernicharo et al., 2021a), the cyano derivatives of cyclopentadiene, benzene and naphthalene (McGuire et al., 2018; McCarthy et al., 2021; Lee et al., 2021; McGuire et al., 2021), the ethynyl derivatives of cyclopentadiene (Cernicharo et al., 2021c), together with the discovery of extremely abundant hydrocarbons such as propargyl (Agúndez et al., 2021a), vinyl acetylene (Cernicharo et al., 2021d), and allenyl acetylene (Cernicharo et al., 2021e) suggest that key chemical processes involving hydrocarbons (radical, neutral, and/or ionic species) were not considered in previous chemical networks. Most of these species were not predicted to have a significant abundance. Hence, a new chemistry is emerging from these observations of TMC-1.

[★] Based on observations carried out with the Yebes 40m telescope (projects 19A003, 20A014, 20D023, and 21A011) and the Institut de Radioastronomie Millimétrique (IRAM) 30m telescope. The 40m radiotelescope at Yebes Observatory is operated by the Spanish Geographic Institute (IGN, Ministerio de Transportes, Movilidad y Agenda Urbana). IRAM is supported by INSU/CNRS (France), MPG (Germany), and IGN (Spain).

TMC-1 is also a source that is particularly rich in sulphur bearing molecules. In addition to the well-known species CS, CCS, and C₃S in this source (Saito et al., 1987; Yamamoto et al., 1987), eight new S-bearing species have been discovered in the last year with the QUIJOTE line survey: HCCCS⁺, NCS, HCCS, H₂CCS, H₂CCCS, C₄S, HCSCN, and HCSCCH (Cernicharo et al., 2021f,g,h). In addition, C₅S, which has previously only been detected in evolved stars, has also been detected in TMC-1 (Cernicharo et al., 2021g). Also complex O-bearing molecules, such as CH₂CHCHO, CH₂CHOH, HCOOCH₃, and CH₃OCH₃, have been detected (Agúndez et al., 2021b) in this cloud. Moreover, the protonated species of tricarbon monoxide and ketene, HC₃O⁺ and CH₃CO⁺, have also been detected recently (Cernicharo et al., 2020a, 2021i). On the other hand, one of the most intriguing results concerning O-bearing species has been the detection of the long carbon chain radicals HC₅O and HC₇O which are particularly abundant (McGuire et al., 2017; Cordiner et al., 2017). Therefore, similar molecules of the type C_nO and HC_nO could be present in TMC-1. The detection of these species could provide insights on the oxygen chemistry in this source.

In this Letter, we report the discovery of the radical HCCCO (trans-propynonyl) and of the O-bearing carbon chain C₅O (pentacarbon monoxide). Line surveys with the Yebes 40m telescope (QUIJOTE¹; see Cernicharo et al. 2021a) and the IRAM 30m ra-

¹ Q-band Ultrasensitive Inspection Journey to the Obscure TMC-1 Environment

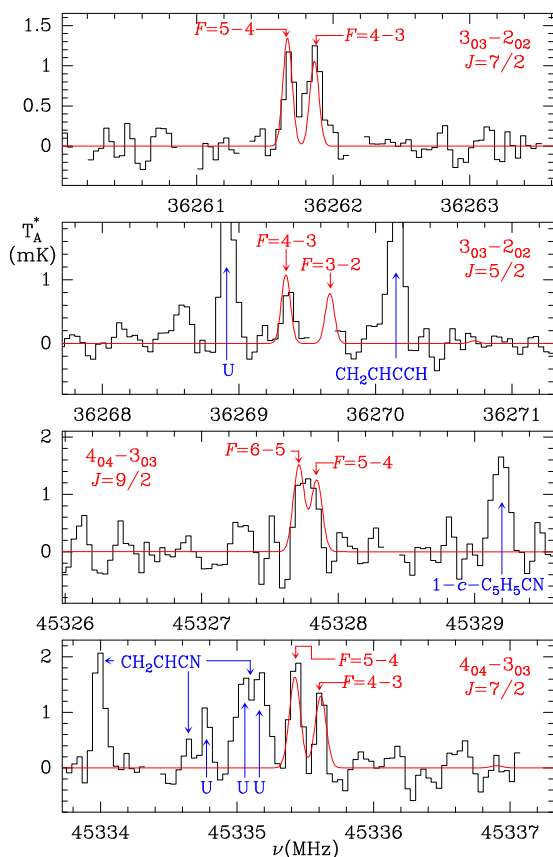


Fig. 1. Observed transitions of HCCCO in TMC-1. The abscissa corresponds to the rest frequency of the lines. Frequencies and intensities for the observed lines are given in Table A.1. The ordinate is the antenna temperature, corrected for atmospheric and telescope losses, in milli Kelvin. The quantum numbers of each transition are indicated in the corresponding panel. The red line shows the computed synthetic spectrum for this species for $T_r=7$ K and a column density of 1.3×10^{11} cm $^{-2}$. Blank channels correspond to negative features produced in the folding of the frequency switching data.

diotelescope have been used for this work. We report a detailed study of the HC $_n$ O and C $_n$ O families of O-bearing species. The formation of these species is investigated with the aid of a chemical model. A robust detection of HC $_5$ O and HC $_7$ O is also presented.

2. Observations

New receivers, built within the Nanocosmos project² and installed at the Yebes 40m radiotelescope, were used for the observations of TMC-1 ($\alpha_{J2000} = 4^{\text{h}}41^{\text{m}}41.9^{\text{s}}$ and $\delta_{J2000} = +25^{\circ}41'27.0''$). A detailed description of the system is given by Tercero et al. (2021). The receiver consists of two cold high electron mobility transistor amplifiers covering the 31.0-50.3 GHz band with horizontal and vertical polarisations. Receiver temperatures in the runs achieved during 2020 vary from 22 K at 32 GHz to 42 K at 50 GHz. Some power adaptation in the down-conversion chains have reduced the receiver temperatures during 2021 to 16 K at 32 GHz and 30 K at 50 GHz. The backends are $2 \times 8 \times 2.5$ GHz fast Fourier transform spectrometers with a spectral resolution of 38.15 kHz, providing the whole coverage of the Q-band in both polarisations. All observations were performed in the frequency switching mode with frequency throws

of 8 and 10 MHz. A detailed description of the QUIJOTE line survey is provided in Cernicharo et al. (2021a). The main beam efficiency varies from 0.6 at 32 GHz to 0.43 at 50 GHz. Pointing corrections were derived from nearby quasars and SiO masers, and errors were always within 2-3". The telescope beam size is 56" and 31" at 31 and 50 GHz, respectively. The intensity scale used in this work, that is to say the antenna temperature (T_A^*), was calibrated using two absorbers at different temperatures and the atmospheric transmission model (ATM; Cernicharo 1985; Pardo et al. 2001). Calibration uncertainties were adopted to be 10 %.

The IRAM 30m data come from a line survey performed towards TMC-1 and B1 and the observations have been described by Marcelino et al. (2007) and Cernicharo et al. (2012). All data were analysed using the GILDAS package³.

3. Results

The sensitivity of our observations towards TMC-1, between 0.19-0.35 mK (1σ), is much larger than previously published line surveys of this source at the same frequencies (Kaifu et al., 2004). In fact, it has been possible to detect many individual lines from molecular species that were previously reported by only stacking techniques (Marcelino et al., 2021; Cernicharo et al., 2021b,c). Line identification in this work has been performed using the MADEX catalogue (Cernicharo , 2012), the Cologne Database of Molecular Spectroscopy (CDMS) catalogue (Müller et al. 2005), and the Jet Propulsion Laboratory (JPL) catalogue (JPL; Pickett et al. 1998).

3.1. First detection of *trans*-propynonyl (HCCCO)

Rotational spectroscopy for this radical is available from the microwave (Chen et al. , 1996) and millimetre and sub-millimetre domains (Cooksy et al. , 1992a,b). Frequency predictions as provided by the CDMS catalogue (Müller et al., 2005) are rather accurate in the 31-50 GHz domain. They have been implemented in the MADEX code. The dipole moment adopted for this species is $\mu_a=2.39$ D (Cooksy et al. , 1995). The ground electronic state of the molecule corresponds to a $^2A'$ quasilinear species. Due to the large A rotational constant, ~ 261 GHz (Cooksy et al. , 1992a), all rotational levels with energies below 12.2 K have $K_a=0$ up to $J=12$. The first $K_a=1$ level is the 1_{11} $J=1/2$ $F=1$, which has an energy of 12.4 K. Hence, the strongest lines for a cold dark cloud with $T_K=10$ K are those connecting levels with $K_a=0$, with weaker emission from $K_a=1$ transitions. Two of the $K_a=0$ rotational transitions, the $3_{03}-2_{02}$ and $4_{04}-3_{03}$, are in the domain of the QUIJOTE line survey and are predicted to have intensities above 1 mK for column densities $\geq 10^{11}$ cm $^{-2}$. These transitions exhibit a fine ($J = N \pm 1/2$) and hyperfine structure, and they have been detected with QUIJOTE. Fig. 1 shows the observed lines and the derived line parameters provided in Table A.1. The averaged v_{LSR} of the lines is 5.75 ± 0.04 km s $^{-1}$, which agrees within 2σ with the value obtained for the cyanopolyynes family of 5.83 ± 0.03 km s $^{-1}$ (Cernicharo et al., 2020b).

The two observed rotational transitions have very close upper level energies and thus cannot provide a reasonable estimate for T_{rot} . Moreover, no collisional rates are available for this species. Hence, in order to derive a column density, we need to assume a rotational temperature. We have assumed the value derived for C $_3$ O in Appendix C.2 ($T_{rot}=7$ K). Adopting a source of uniform brightness and a diameter of 80" (Fossé et al., 2001), which

² <https://nanocosmos.iff.csic.es/>

³ <http://www.iram.fr/IRAMFR/GILDAS>

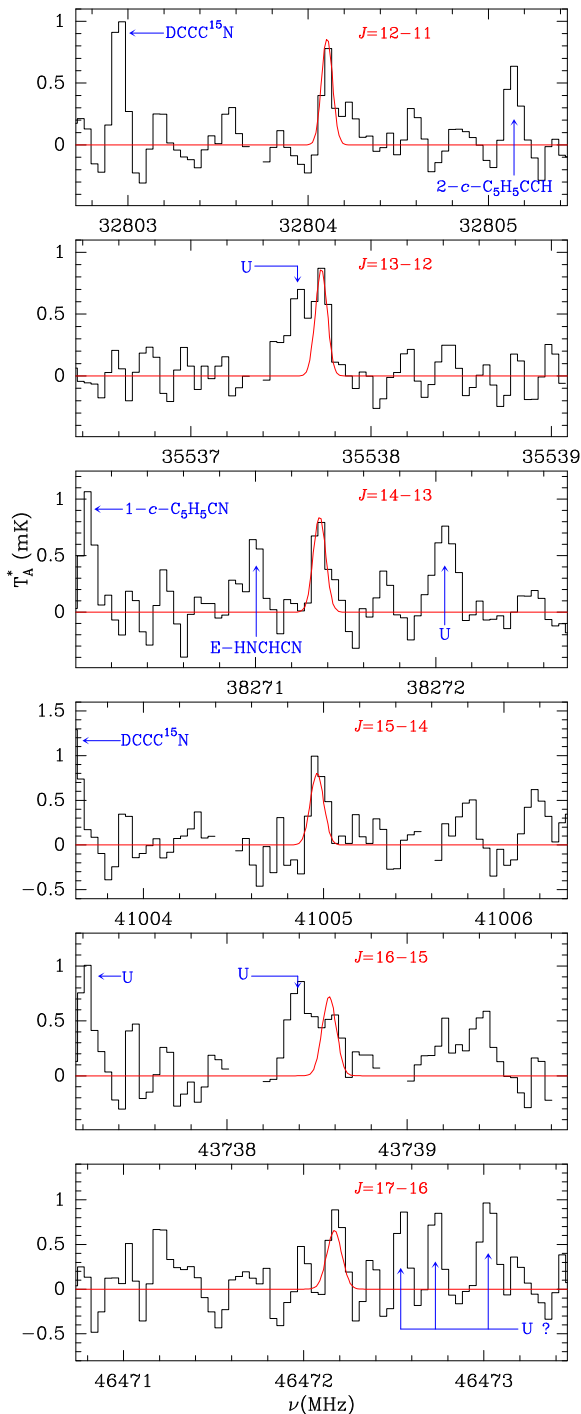


Fig. 2. Similar to Fig. 1, but for the observed transitions of C₅O in TMC-1. The red line shows the computed synthetic spectrum for this species for $T_r=10$ K and a column density of 1.5×10^{10} cm⁻².

means that the source practically fills the beam at all of the frequencies of the survey, we derived a column density for HCCCO of $(1.3 \pm 0.2) \times 10^{11}$ cm⁻². The column densities of other members of the HC_nO family are derived in Appendix B and are given in Table 1. We note that HC₅O appears to be the most abundant species of the HC_nO family of O-bearing carbon chains, with a relative abundance of 1.3 ± 0.3 , 1.8 ± 0.3 , 11 ± 3 , and 2.2 ± 0.3 with respect to HCO, HCCO, HC₃O, and HC₇O, respectively. Also, HC₄O and HC₆O have been searched, but only upper limits have been obtained (see Appendix B.3).

3.2. First detection of pentacarbon monoxide (C₅O)

The O-bearing chains CCO and C₃O have been observed in TMC-1 with large column densities (see Appendices C.1 and C.2). Hence, other similar chains such as C₄O, C₅O, and C₆O could be present in this cloud.

We note that C₅O has been observed in the microwave laboratory up to 24.6 GHz and $J_{max}=9$ by Ogata et al. (1995). The uncertainty of the frequency measurements is 1 kHz. We adopted a dipole moment of 4.06 D as derived by Botschwina et al. (1995) from ab initio calculations. Six lines of C₅O from $J = 12 - 11$ up to $J = 17 - 16$ are clearly detected at a v_{LSR} of 5.38-5.66 km s⁻¹. They are shown in Fig. 2. All the lines of C₅O are shifted by 15-40 kHz with respect to the predictions if a v_{LSR} of 5.75 km s⁻¹ is adopted. This velocity is the average value of the v_{LSR} velocities observed for the lines of HC-CCO, CCO, C₃O, HC₅O, and HC₇O (see Table A.1 and Appendices B, C). Consequently, we adopted a velocity of 5.75 km s⁻¹ to derive the rest frequencies of the observed lines of C₅O. We merged them with the laboratory data of Ogata et al. (1995) to derive improved rotational and distortion constants. The obtained values are $B=1366.847016 \pm 0.000058$ MHz and $D=0.03413 \pm 0.00045$ kHz, while the laboratory data alone provide $B=1366.847112 \pm 0.000065$ MHz and $D=0.03509 \pm 0.00056$ kHz.

A rotational diagram of the observed lines of C₅O provides a rotational temperature of 10 ± 0.5 K and a column density of $(1.5 \pm 0.2) \times 10^{10}$ cm⁻². In order to check the excitation conditions for the rotational lines of this species, we assumed that the collisional rates of C₅O could be similar to those of HC₅N with *p*-H₂ (kindly provided by Francois Lique, private communication). For a linewidth of 0.6 km s⁻¹, a volume density of 4×10^4 cm⁻³ (Cernicharo & Guélin, 1987; Fossé et al., 2001), and a kinetic temperature of 10 K, large velocity gradient (LVG) calculations performed with the MADEX code indicate that all rotational lines up to $J_u=20$ will have excitation temperatures close to thermalisation (between 9.5 and 10 K). This result is similar to that obtained for HC₅N and its isotopologues from the data in our line survey (Cernicharo et al., 2020b). The synthetic spectra computed with a rotational temperature of 10 K and the column density derived from the rotational diagram are shown in Fig. 2 and are in excellent agreement with observations.

Assuming a column density for H₂ of 10^{22} cm⁻² (Cernicharo & Guélin, 1987), we derived an abundance for C₅O of 2×10^{-12} . This is 50 ± 15 and 80 ± 20 times lower than that of CCO and C₃O, respectively (see Appendices C.1, C.2, and Table 1). We searched for the species C₄O and C₆O (see Appendix C.3), but only upper limits have been obtained. They are given in Table 1. It is important to note that C₃O appears to be the most abundant species of the C_nO family ($n \geq 2$).

4. Discussion

The derived abundance for the different members of the C_nO ($n \geq 2$) and HC_nO ($n \geq 1$) families permit one to study the possible routes for their formation. It is worth noting that HC₅O is the more abundant species of both series, and that the heavy species HC₇O is only slightly lower in abundance. This is a peculiar result indeed as it is clearly opposite to the behaviour of the HC_{2n+1}N family, where the abundance decreases with *n*, and the different molecules are formed by the consecutive addition of CCH or CN (Cernicharo et al., 1987; Agúndez et al., 2008). Nevertheless, the peculiarities of HC₅O and HC₇O are not restricted to the physical conditions of interstellar clouds. In the

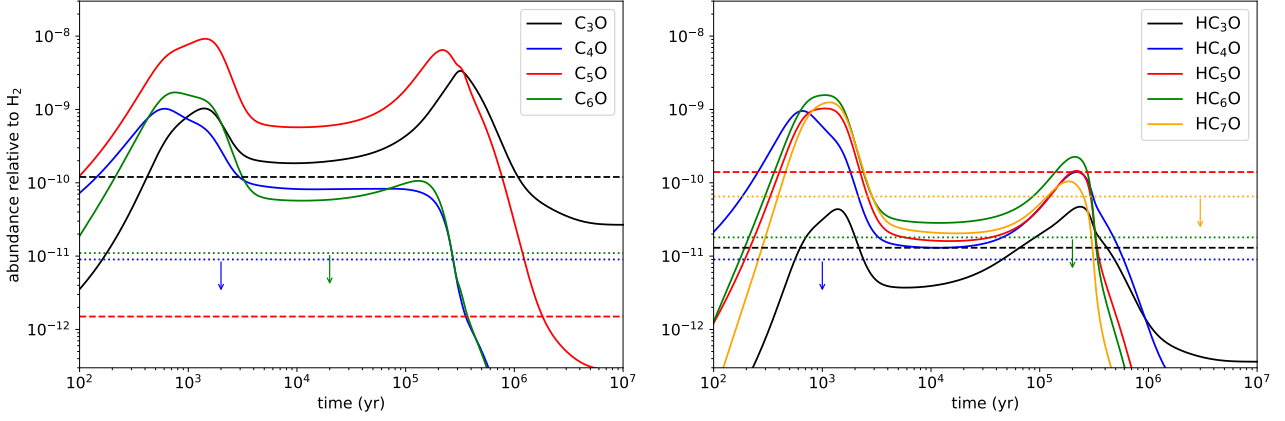
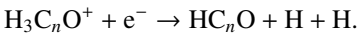
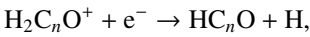
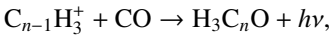
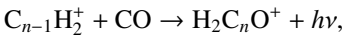
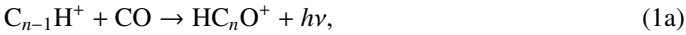


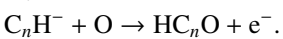
Fig. 3. Calculated fractional abundances for several C_nO and HC_nO species as a function of time. Observed abundances in TMC-1 are indicated by horizontal dashed lines, while horizontal dotted lines represent upper limits for non-detected species.

laboratory experiments devoted to the rotational characterisation of these molecules, Mohamed et al. (2005) reported that HC_5O was the most abundant species generated in their discharges for different precursors. In the Stardust and AROMA experimental setups of the Nanocosmos project (Martínez et al. , 2020; Santoro et al. , 2020; Sabbah et al. , 2017), it has been observed that in experiments using pure carbon as a seed for the growth of nanoparticles, masses associated with HC_5O and HC_7O are clearly detected, with that of HC_7O being rather prominent and comparable in intensity to C_7H_2 (Martínez et al. , 2020). In similar experiments, but adding C_2H_2 to the growth chamber, HC_3O , HC_5O , and HC_7O are also detected. The source of the oxygen for the formation of these molecules is probably related to air contamination (O_2) during transportation of the samples (Martínez et al. , 2020; Santoro et al. , 2020). No other oxidised molecules were detected in these experiments. Although the physical conditions between the interstellar clouds and these experiments are very different, it seems that these molecules are easily formed under a variety of conditions.

Two main mechanisms have been proposed to account for the formation of C_nO and HC_nO species in interstellar space. The first involves the radiative association of $C_{n-1}H^+$, $C_{n-1}H_2^+$, and $C_{n-1}H_3^+$ ions with CO (Adams et al. , 1989), followed by dissociative recombination with electrons,



The second consists of direct formation through reactions of C_n^- and C_nH^- anions with O atoms (Eichelberger et al. , 2007; Cordiner & Charnley , 2012),



The two mechanisms have problems reproducing some of the abundances observed for C_nO and HC_nO in TMC-1. McGuire et al. (2017) implemented the mechanism (1) in a chemical model and found that the abundance HC_4O is overestimated by at least two orders of magnitude, while including the two mechanisms

(1) and (2) resulted in an overestimation of the abundances of HC_6O , C_6O , and C_7O by at least one or two orders of magnitude (Cordiner & Charnley , 2012; Cordiner et al. , 2017).

Here we included the reactions relevant for mechanisms (1) and (2) in a chemical model of a cold dark cloud similar to those presented in previous studies of TMC-1 (e.g. Agúndez et al. 2021a). We adopted rate coefficients for radiative associations in scheme (1a) from Adams et al. (1989); for dissociative recombinations in scheme (1b) from the estimations of Loison et al. (2017) for HC_3O^+ , $H_2C_3O^+$, and $H_3C_3O^+$; and for reactions of negative ions with O atoms in scheme (2) from Eichelberger et al. (2007) and Cordiner & Charnley (2012). We assume that C_nO and HC_nO species react with the most abundant cations (H^+ , C^+ , He^+ , HCO^+ , and H_3O^+) and with C atoms, but we consider that only open shell species (all HC_nO species and C_nO with n even) react with H, N, and O atoms.

The results are shown in Fig. 3. The observed abundances of HC_3O , HC_5O , and HC_7O are reasonably reproduced. However, HC_4O and HC_6O are overestimated by one order of magnitude. That is, the chemical model does not make a strong differentiation between HC_nO species with an even n and an odd n , in contrast to observations which indicate that HC_nO species with n odd are favoured. Concerning the carbon chains C_nO , the chemical model predicts a clear differentiation between C_nO with an even n and an odd n , as a result of the different reactivity with H, N, and O atoms. However, the calculated abundances are too large. This is especially dramatic in the case of C_5O , whose calculated abundance is almost four orders of magnitude too high. The chemical mechanisms (1) and (2) are too efficient at producing O-bearing carbon chains, and they lack specificity between an even n and an odd n for HC_nO species. The assumptions behind these mechanisms must be revised, in particular the rate coefficients adopted for the radiative associations in scheme (1a) and the branching ratios leading to C_nO in the reactions between C_n^- and O atoms in scheme (2). In addition, it would be desirable to know the true low-temperature reactivity of these O-bearing carbon chains with neutral atoms.

The overabundance of some of the C_nO and HC_nO species in the chemical model including the chemical mechanisms (1) and (2), together with the fact that HC_3O , HC_5O , and HC_7O are observed in the Nanocosmos experiments, suggest that other chemical routes may be behind the formation of these species. In particular, the reactions of C_n and C_nH carbon chains with O atoms and the radicals OH and HCO are potential sources of C_nO and HC_nO species. The alternation in the abundances of

Table 1. Column densities for relevant O-bearing species in TMC-1

Molecule	N^a	T_{rot}^b	X^c
C ₂ O	$(7.5\pm 0.3)\times 10^{11}$	$7-10.0^d$	7.5×10^{-11}
C ₃ O	$(1.2\pm 0.2)\times 10^{12}$	7.0 ± 1.0	1.2×10^{-10}
C ₄ O	$\leq 9.0\times 10^{10}$	10.0	$\leq 9.0\times 10^{-12}$
C ₅ O	$(1.5\pm 0.2)\times 10^{10}$	10.0 ± 0.5	1.5×10^{-12}
C ₆ O	$\leq 1.1\times 10^{11}$	10.0	$\leq 1.1\times 10^{-11}$
HCO	$(1.1\pm 0.1)\times 10^{12}$	7.0	1.1×10^{-10}
HC ₂ O	$(7.7\pm 0.7)\times 10^{11}$	7.0	7.7×10^{-11}
HC ₃ O	$(1.3\pm 0.2)\times 10^{11}$	7.0	1.3×10^{-11}
HC ₄ O	$\leq 9.0\times 10^{10}$	10.0	$\leq 9.0\times 10^{-12}$
HC ₅ O	$(1.4\pm 0.2)\times 10^{12}$	10.0	1.4×10^{-10}
HC ₆ O	$\leq 1.8\times 10^{11}$	10.0	$\leq 1.8\times 10^{-11}$
HC ₇ O	$(6.5\pm 0.5)\times 10^{11}$	10.0	6.5×10^{-11}

Notes.

(^a) Column density in cm⁻². Upper limits correspond to 3 σ values.

(^b) Rotational temperature. When the uncertainty is not provided, it corresponds to an assumed value.

(^c) Relative abundance to H₂, assuming a total column density of molecular hydrogen of 10²² cm⁻² (Cernicharo & Guélin, 1987).

(^d) Column density derived from a large velocity gradient model (see Appendix C.1).

consecutive C_nH radicals, with those with n even being more abundant than those with n odd, could produce, in their reaction with HCO, a similar behaviour for the HC_nO species in which case those with n odd would be more abundant than those with n even. However, little is known about these reactions.

5. Conclusions

We detected, for the first time in space, the species HC₃O and C₅O. In addition, we have provided an exhaustive list of abundances and upper limits for O-bearing carbon chains C_nO and HC_nO in TMC-1. The species with n odd are found to be more abundant than those with n even. In particular, C₃O and HC₅O are especially abundant. Formation mechanisms for these species based on radiative associations of C_nH_m⁺ ions with CO and reactions between C_n⁻ and C_nH⁻ anions with O atoms reproduce some features, but result in abundances that are too large for some species such as C₅O, HC₄O, and HC₆O. Alternative chemical routes for these species involving neutral-neutral reactions should be explored.

Acknowledgements. We thank Ministerio de Ciencia e Innovación of Spain (MCIU) for funding support through projects PID2019-106110GB-I00, PID2019-107115GB-C21 / AEI / 10.13039/501100011033, and PID2019-106235GB-I00. We also thank ERC for funding through grant ERC-2013-SyG-610256-NANOCOSMOS. M.A. thanks MCIU for grant RyC-2014-16277. We would like to thank C. Joblin for her useful comments on the laboratory experiments of formation of carbon dust analogues in which HC₃O, HC₅O and HC₇O are observed. We would like also to thank Evelyn Roueff and Octavio Roncero for useful comments on the possible reactions leading to the formation of HC_nO.

References

Adams, N.G., Smith, D., Giles, K. & Herbst, E. 1989, A&A, 220, 269
 Agúndez, M., Fonfrá, J.P., Cernicharo, et al. 2008, A&A, 479, 493
 Agúndez, M., Cernicharo, J. & Guélin, M. 2015, A&A, 577, L5
 Agúndez, M., Cabezas, C., Tercero, B., et al. 2021a, A&A, 647, L10
 Agúndez, M., Marcelino, N., Tercero, B. et al. 2021b, A&A, 649, L4
 Alexander, M.H. & Dalgarno, P.J. 1983, J. Chem. Phys., 79, 302
 Austin, J.A., Levy, D.H., Gottlieb, C.A., & Radford, H.E. 1974, J. Chem. Phys., 60, 207
 Bizzocchi, L., Degli Esposti, C., Dore, L., 2008, A&A, 492, 875
 Blake, G.A., Sastry, K.V.L.N., de Lucia, F.C. 1984, J. Chem. Phys., 80, 95

Bogey, M., Demuyck, C., Destombes, J.L., & Lapauw, J.M., 1986, J. Phys. E: Sci. Instr., 19, 520
 Botschwina, P., Flügge, J. & Sebald, P. 1995, J. Phys. Chem., 99, 9755
 Brown, R.D., Eastwood, F.W., Elmes, P.S., & Godfrey, P.D. 1983, J. Am. Chem. Soc. 105, 6496
 Brown, R.D., Godfrey, P.D., Cragg, D.M., & Rice, E.H.N. 1985, ApJ, 297, 302
 Cernicharo, J. 1985, Internal IRAM report (Granada: IRAM)
 Cernicharo, J. & Guélin, M. 1987, A&A, 176, 299
 Cernicharo, J., Guélin, M., Menten, K., & Walmsley, C.M., 1987, A&A, 181, L1
 Cernicharo, J., 2012, in ECLA 2011: Proc. of the European Conference on Laboratory Astrophysics, EAS Publications Series, 2012, Ed.: C. Stehl, C. Joblin, & L. d'Hendecourt (Cambridge: Cambridge Univ. Press), 251; https://nanocosmos.iff.csic.es/?page_id=1619
 Cernicharo, J., Marcelino, N., Roueff, E. et al. 2012, ApJ, 759, L43
 Cernicharo, J., Marcelino, N., Agúndez, M., et al. 2020a, A&A, 642, L17
 Cernicharo, J., Marcelino, N., Agúndez, et al. 2020b, A&A, 642, L8
 Cernicharo, J., Agúndez, M., Kaiser, R.I. et al. 2021a, A&A, 652, L9
 Cernicharo, J., Agúndez, M., Cabezas, C. et al. 2021b, A&A, 649, L15
 Cernicharo, J., Agúndez, M., Kaiser, R.I. et al. 2021c, A&A, arXiv:2110.09105
 Cernicharo, J., Agúndez, M., Cabezas, C., et al. 2021d, A&A, 648, L2
 Cernicharo, J., Cabezas, C., Agúndez, M. et al. 2021e, A&A, 647, L3
 Cernicharo, J., Cabezas, C., Endo, Y., et al. 2021f, A&A, 646, L3
 Cernicharo, J., Cabezas, C., Agúndez, M., et al. 2021g, A&A, 648, L3
 Cernicharo, J., Cabezas, C., Endo, Y. et al. 2021h, A&A, 650, L14
 Cernicharo, J., Cabezas, C., Baillieux, S., et al. 2021i, A&A, 646, L7
 Chantzos, J., Spezzano, S., Endres, C. et al. 2019, A&A, 621, A111
 Chen, W., Novick, S.E., McCarthy, M.C., et al. 1996, ApJ, 462, 562
 Cooksy, A.L., Watson, J.K.G., Gottlieb, C.A. & Thaddeus, P. 1992a, ApJ, 386, L27
 Cooksy, A.L., Watson, J.K.G., Gottlieb, C.A. & Thaddeus, P. 1992b, J. Mol. Spectrosc., 153, 610
 Cooksy, A.L., Tao, F.M., Klemperer, W., & Thaddeus, P. 1995, J. Phys. Chem., 99, 11095
 Cordiner, M.A. & Charnley, S.B. 2012, ApJ, 749, 120
 Cordiner, M.A., Charnley, S.B., Kisiel, Z., et al., 2017, ApJ, 850, 187
 Corey, G.C. & McCourt, F.R. 1983, J. Chem. Phys., 87, 2723
 Eichelberger, B., Snow, T.P., Barckholtz, C., Bierbaum, V.M. 2007, ApJ, 667, 1283
 Endo, Y. & Hirota, E. 1987, J. Chem. Phys., 86, 4319
 Faure, A., Lique, F. & Wiesenfeld, L. 2016, MNRAS, 460, 2103
 Fossé, D., Cernicharo, J., Gerin, M., Cox, P. 2001, ApJ, 552, 168
 Fuente, A., Cernicharo, J., Barcia, A. & Gómez-González, J. 1990, A&A, 231, 151
 Goldreich, P., Kwan, J. 1974, ApJ, 189, 441
 Green, S. & Chapman, S. 1978, ApJS, 37, 169
 Kaifu, N., Ohishi, M., Kawaguchi, K., et al. 2004, PASJ, 56, 69
 Klebsch, W., Bester, M., Yamada, K.M.T., et al. 1985, A&A, 152, L12
 Lee, K.L.K., Changala, P.B., Loomis, R.A., et al. 2021, ApJ, 910, L2
 Loison, J.-C., Agúndez, M., Wakelam, V., et al. 2017, MNRAS, 470, 4075
 Marcelino, N., Cernicharo, J., Agúndez, M., et al. 2007, ApJ, 665, L127
 Marcelino, N., Tercero, B., Agúndez, M., & Cernicharo, J. 2021, A&A, 646, L9
 Martínez, L., Lauwaet, K., Santoro, G., et al. 2020, NatSR, 8, 7250
 Matthews, H.E., Irvine, W.M., Friberg, P., et al. 1984, Nature, 310, 125
 McCarthy, M.C., Lee, K.L.K., Loomis, R.A., et al. 2021, Nature Astron., 5, 176
 McGuire, B.A., Burkhardt, A.M., Shingledecker, C.N., et al. 2017, ApJ, 843, L28
 McGuire, B.A., Burkhardt, A.M., Kalenskii, S., et al. 2018, Science, 359, 202
 McGuire, B.A., Loomis, R.A., Burkhardt, A.M., et al. 2021, Science, 371, 1265
 Mohamed, S., McCarthy, M.C., Cooksy, A.L., et al. 2005, J. Chem. Phys., 123, 234301
 Müller, H.S.P., Schlöder, F., Stutzki, J., Winnewisser, G. 2005, J. Mol. Struct., 742, 215
 Ogata, T., Ohshima, Y. & Endo, Y. 1995, J. Am. Chem. Soc., 117, 3593
 Ohishi, M., Suzuki, H., Ishikawa, S.I., et al. 1991, ApJ, 380, L39
 Ohshima, Y. & Endo, Y. 1993, J. Mol. Spectrosc., 159, 458
 Ohshima, Y., Endo, Y. & Ogata 1995, J. Chem. Phys., 102, 1493
 Pardo, J. R., Cernicharo, J., Serabyn, E. 2001, IEEE Trans. Antennas and Propagation, 49, 12
 Pickett, H.M. & Boyd, T.L. 1978, Chem. Phys. Lett., 58, 446
 Pickett, H.M., Poynter, R. L., Cohen, E. A., et al. 1998, J. Quant. Spectrosc. Radiat. Transfer, 60, 883
 Sabbah, H., Bonnamy, A., Papanastasiou, D., et al. 2017, ApJ, 843, 34
 Saito, S. 1972 ApJ, 178, L95
 Saito, S., Kawaguchi, K., Yamamoto, S., et al. 1987, ApJ, 317, L115
 Santoro, G., Martínez, L., Lauwaet, K., et al. 2020, ApJ, 895, 97
 Szalay, P.G., Fogarasi, G. & Nemes, L. 1996, Chem. Phys. Lett., 263, 91
 Tang, T.B., Inokuchi, H., Saito, S., et al. 1985, Chem. Phys. Lett. 116, 83
 Tenenbaum, E.D., Apponi, A.J., Ziurys, L.M., et al. 2006, ApJ, 649, L17
 Tercero, F., López-Pérez, J. A., Gallego, et al. 2021, A&A, 645, A37
 Thomson, C. & Wishart, B.J. 1973, Theor. Chim. Acta, 31, 347
 Urso, R.G., Palumbo, M.E., Ceccarelli, C., et al. 2019, A&A, 629, A72
 Yamada, C., Saito, S., Kanamori, H. & Hirota, E. 1985, ApJ, 290, L65
 Yamamoto, S., Saito, S., Kawaguchi, K. et al. 1987, ApJ, 317, L119

Appendix A: Observed line parameters

Line parameters for the different molecules studied in this work were obtained by fitting a Gaussian line profile to the observed data. A window of $\pm 15 \text{ km s}^{-1}$ around the v_{LSR} of the source was considered for each transition. The derived line parameters for all the molecular species studied in this work are given in Table A.1.

Table A.1. Observed line parameters for the species studied in this work

Transition	ν_{rest}^a (MHz)	$\int T_A^* dv^b$ (mK km s $^{-1}$)	Δv^c (km s $^{-1}$)	Δv^d (km s $^{-1}$)	T_A^{*e} (mK)	
HCCO¹						
4 _{0,4} – 3 _{0,3} 9/2-7/2 5-4	36261.666±0.004	0.90±0.12	5.73±0.04	0.74±0.11	1.14±0.15	
4 _{0,4} – 3 _{0,3} 9/2-7/2 4-3	36261.863±0.004	1.41±0.14	5.83±0.05	1.15±0.15	1.14±0.15	
4 _{0,4} – 3 _{0,3} 7/2-5/2 4-3	36269.344±0.003	0.75±0.14	5.66±0.08	0.82±0.16	0.85±0.15	
4 _{0,4} – 3 _{0,3} 7/2-5/2 3-2	36269.666±0.003					A
5 _{0,5} – 4 _{0,4} 11/2-9/2 6-5	45327.712±0.004	0.63±0.19	5.74±0.20	0.60	0.99±0.22	B
5 _{0,5} – 4 _{0,4} 11/2-9/2 5-4	45327.843±0.004	0.61±0.18	5.92±0.20	0.60	0.96±0.22	B
5 _{0,5} – 4 _{0,4} 9/2-7/2 5-4	45335.424±0.004	1.35±0.15	5.79±0.04	0.62±0.07	2.06±0.22	
5 _{0,5} – 4 _{0,4} 9/2-7/2 4-3	45335.613±0.004	0.73±0.13	5.82±0.05	0.44±0.09	1.57±0.22	
CCO²						
1 ₁ – 0 ₁	32623.449±0.007	2.71±0.30	5.53±0.05	0.87±0.11	2.94±0.27	
2 ₁ – 1 ₁	32738.613±0.005	1.23±0.23	5.73±0.06	0.70±0.13	1.65±0.24	
2 ₃ – 1 ₂	45826.734±0.002	9.11±0.47	5.75±0.07	0.75±0.03	11.36±0.46	
2 ₂ – 1 ₁	46182.187±0.002	2.73±0.30	5.70±0.03	0.49±0.07	5.26±0.44	
4 ₅ – 3 ₄	92227.870±0.003	6.34±0.35	5.71±0.03	0.53±0.09	11.34±1.53	
4 ₄ – 3 ₃	92363.257±0.004	3.37±0.47	5.64±0.05	0.32±0.05	11.06±1.37	
4 ₃ – 3 ₂	92718.775±0.003	4.31±0.38	5.73±0.03	0.64±0.07	6.29±0.80	
C₃O³						
4-3	38486.891±0.001	38.76±0.34	5.74±0.01	0.59±0.01	61.78±0.43	
5-4	48108.474±0.001	40.83±0.15	5.74±0.01	0.65±0.01	58.61±0.23	
8-7	76972.587±0.001	30.31±0.53	5.75±0.01	0.55±0.01	51.56±1.10	
9-8	86593.685±0.001	17.30±1.40	5.75±0.02	0.41±0.04	39.26±3.00	
10-9	96214.614±0.001	8.47±0.22	5.75±0.01	0.50±0.02	16.07±0.55	
11-10	105835.358±0.002	4.85±0.71	5.78±0.03	0.38±0.07	12.04±2.30	
C₅O^{3,4}						
12-11	32804.100±0.010	0.69±0.21	5.75	0.57±0.19	0.68±0.17	
13-12	35527.730±0.010	0.53±0.15	5.75	0.51±0.20	0.97±0.18	
14-13	38271.346±0.010	0.55±0.13	5.75	0.67±0.19	0.78±0.18	
15-14	41004.959±0.020	0.79±0.14	5.75	0.69±0.13	1.07±0.22	
16-15	43738.562±0.030	0.57±0.19	5.75	0.95±0.33	0.56±0.23	
17-16	46472.169±0.030	0.42±0.12	5.75	0.56±0.11	0.96±0.26	
HCO¹						
1 ₀₁ – 0 ₀₀ 3/2-1/2 2-1	86670.760±0.060	42.52±1.97	5.94±0.02	0.66±0.04	60.69±3.91	
1 ₀₁ – 0 ₀₀ 3/2-1/2 1-0	86708.360±0.040					C
1 ₀₁ – 0 ₀₀ 1/2-1/2 1-1	86777.460±0.040	23.94±1.67	5.90±0.02	0.60±0.06	37.57±3.10	
1 ₀₁ – 0 ₀₀ 1/2-1/2 0-1	86805.780±0.100	11.84±1.70	5.95±0.04	0.58±0.10	19.25±3.27	
HCCO¹						
2 ₀₂ – 1 ₀₁ 5/2-3/2 3-2	43317.667±0.004	5.80±0.19	5.71±0.02	0.68±0.03	8.00±0.22	
2 ₀₂ – 1 ₀₁ 5/2-3/2 2-1	43321.145±0.004	4.22±0.27	5.66±0.04	0.92±0.08	4.30±0.22	
2 ₀₂ – 1 ₀₁ 3/2-1/2 2-1	43329.542±0.003	5.07±0.26	5.69±0.02	0.73±0.04	6.56±0.22	
2 ₀₂ – 1 ₀₁ 3/2-1/2 1-0	43335.463±0.004	2.23±0.25	5.70±0.08	0.98±0.13	2.14±0.22	
2 ₀₂ – 1 ₀₁ 5/2-3/2 2-2	43336.861±0.004	0.98±0.25	5.66±0.08	0.63±0.15	1.45±0.22	
2 ₀₂ – 1 ₀₁ 3/2-3/2 1-1	43337.304±0.006	1.54±0.23	5.67±0.08	0.75±0.15	1.93±0.22	
4 ₀₄ – 3 ₀₃ 9/2-7/2 5-4	86642.342±0.006	3.16±1.00	5.64±0.08	0.22±0.11	13.71±3.80	
4 ₀₄ – 3 ₀₃ 9/2-7/2 4-3	86643.848±0.005	4.27±1.09	5.67±0.08	0.26±0.11	15.31±3.80	
4 ₀₄ – 3 ₀₃ 7/2-5/2 4-3	86655.831±0.005	7.23±1.45	5.69±0.08	0.40±0.13	16.97±3.80	
4 ₀₄ – 3 ₀₃ 7/2-5/2 3-2	86657.485±0.005	2.96±0.97	5.64±0.12	0.24±0.12	11.80±3.80	
HC₃O³						
25/2-23/2 e 13-12	32267.964±0.002	3.86±0.42	5.75±0.03	0.67±0.06	5.38±0.19	
25/2-23/2 e 12-11	32268.049±0.002	4.08±0.42	5.75±0.04	0.75±0.06	5.10±0.19	
25/2-23/2 f 13-12	32271.760±0.002	4.11±0.29	5.67±0.03	0.75±0.05	5.14±0.19	
25/2-23/2 f 12-11	32271.848±0.002	3.21±0.30	5.72±0.02	0.65±0.06	5.38±0.19	
27/2-25/2 e 14-13	34849.461±0.002	4.15±0.11	5.74±0.01	0.60	6.49±0.19	D
27/2-25/2 e 13-12	34849.540±0.002	3.18±0.11	5.73±0.02	0.60	4.99±0.19	D
27/2-25/2 f 14-13	34853.387±0.002	3.55±0.09	5.71±0.01	0.60	5.55±0.19	D
27/2-25/2 f 13-12	34854.469±0.002	2.79±0.10	5.67±0.01	0.60	4.37±0.19	D
29/2-27/2 e 15-14	37430.945±0.003	3.67±0.15	5.74±0.02	0.60	5.74±0.21	D
29/2-27/2 e 14-13	37431.020±0.003	3.42±0.14	5.73±0.02	0.60	5.35±0.21	D
29/2-27/2 f 15-14	37435.011±0.003	3.70±0.14	5.72±0.02	0.60	5.79±0.21	D

Table A.1. continued.

Transition	ν_{rest}^a (MHz)	$\int T_A^* dv^b$ (mK km s ⁻¹)	$\Delta\nu^c$ (km s ⁻¹)	$\Delta\nu^d$ (km s ⁻¹)	T_A^{*e} (mK)	
29/2-27/2 <i>f</i> 14-13	37435.088±0.003	3.29±0.14	5.70±0.02	0.60	5.14±0.21	D
31/2-29/2 <i>e</i>	40012.451±0.004	6.25±0.19	5.73±0.01	0.94±0.03	6.26±0.25	
31/2-29/2 <i>f</i>	40016.669±0.004	6.13±0.19	5.73±0.02	0.95±0.03	6.05±0.25	
33/2-31/2 <i>e</i>	42593.906±0.005	4.76±0.17	5.75±0.02	0.89±0.04	5.03±0.23	
33/2-31/2 <i>f</i>	42598.284±0.005	5.42±0.17	5.75±0.02	0.90±0.03	5.69±0.23	
35/2-33/2 <i>e</i>	45175.347±0.005	4.88±0.23	5.79±0.02	0.87±0.04	5.31±0.28	
35/2-33/2 <i>f</i>	45179.895±0.005	5.51±0.26	5.77±0.02	1.00±0.06	5.20±0.28	
37/2-35/2 <i>e</i>	47746.772±0.007	3.59±0.33	5.82±0.04	0.71±0.09	4.36±0.30	
37/2-35/2 <i>f</i>	47761.502±0.007	3.89±0.36	5.72±0.04	0.72±0.07	5.05±0.30	
HC₇O⁵						
57/2-55/2 <i>e</i>	31274.822±0.003	0.90±0.25	5.81±0.08	0.84±0.21	1.01±0.19	
57/2-55/2 <i>f</i>	31276.500±0.003	1.05±0.15	5.89±0.06	0.78±0.12	1.28±0.19	
59/2-57/2 <i>e</i>	32372.184±0.003					E
59/2-57/2 <i>f</i>	32373.871±0.003	1.29±0.10	5.89±0.04	0.87±0.08	1.39±0.19	
61/2-59/2 <i>e</i>	33469.542±0.004	1.02±0.11	6.00±0.04	0.74±0.02	1.30±0.20	
61/2-59/2 <i>f</i>	33471.241±0.004					E
63/2-61/2 <i>e</i>	34566.898±0.004					F
63/2-61/2 <i>f</i>	34568.607±0.004	0.53±0.08	5.73±0.08	0.65±0.16	0.76±0.20	
65/2-63/2 <i>e</i>	35664.244±0.005	0.37±0.07	5.78±0.18	0.58±0.21	0.59±0.18	
65/2-63/2 <i>f</i>	35665.972±0.005	0.54±0.07	5.68±0.25	1.22±0.32	0.43±0.18	
67/2-65/2 <i>e</i>	36761.602±0.005	0.43±0.12	5.49±0.16	1.11±0.35	0.41±0.21	
67/2-65/2 <i>f</i>	36763.333±0.005	0.59±0.10	5.69±0.07	0.79±0.12	0.70±0.21	
69/2-67/2 <i>e</i>	37858.949±0.005	0.33±0.10	6.00±0.12	0.43±0.25	0.71±0.23	
69/2-67/2 <i>f</i>	37860.691±0.005	0.55±0.13	6.04±0.09	0.74±0.19	0.70±0.23	

Notes.

^(a) Rest frequency of the transition. See text for the laboratory data used for the frequency predictions of each molecular species.

^(b) Integrated line intensity in mK km s⁻¹.

^(c) v_{LSR} in km s⁻¹.

^(d)

Linewidth at half intensity derived by fitting a Gaussian function to the observed line profile (in km s⁻¹).

^(e) Antenna temperature in milli Kelvin.

⁽¹⁾ Quantum numbers are $N, K_a, K_c, J,$ and F .

⁽²⁾ Quantum numbers are N and J .

⁽³⁾ The quantum number is J .

⁽⁴⁾ Improved rest frequencies were derived assuming a v_{LSR} of 5.75 km s⁻¹ (see Sect. 3.2).

⁽⁵⁾ Quantum numbers are J, Λ -doubling component, and F . If the hyperfine structure is not resolved in our data, then F is not given. In this case, the adopted rest frequency corresponds to the average of those of the hyperfine components.

^(A) This line is contaminated by the frequency switching negative feature of the transition $4_{0,4} - 3_{0,3} 9/2-7/2 5-4$ of the same species after data folding since they are separated by exactly 8.0 MHz, i.e. the frequency throw used in the observations.

^(B) This doublet appears unresolved in our data (see Fig. 1). The linewidth has been fixed to 0.6 km s⁻¹. The resulting frequencies and intensities have slightly larger uncertainties than those of other transitions for this molecule.

^(C) The $J=3/2-1/2 F=1-0$ component is heavily blended with the $J=15-14$ transition of C₃S avoiding a reliable determination of the line parameters (see Fig. B.1).

^(D) The hyperfine components are only partially resolved. To obtain reliable parameters for each hyperfine component, their linewidths are fixed to 0.6 km s⁻¹.

^(E) Heavily affected by a negative feature produced in the folding of the frequency switching data (see Fig. B.4).

^(F) This transition is heavily blended with the $J=31-30$ transition of HC₆¹³CN at 34566.972 MHz, which has an intensity of 2.1 mK (see Fig. B.4)

Appendix B: HC_nO species

Appendix B.1: HCO

The HCO radical has an electronic ground state $^2A'$ and has been observed in the laboratory by different authors (Saito , 1972; Austin et al. , 1974; Pickett & Boyd , 1978; Blake et al. , 1984). Frequency predictions are available in the JPL catalogue (Pickett et al. , 1998). We implemented the molecule in the MADEX catalogue and searched for its lines in our 3mm line survey of TMC-1. No lines of HCO appear in the QUIJOTE line survey. Four hyperfine components of the $I_{01}-0_{00}$ transition are detected and they are shown in Fig. B.1. Their line parameters are given in Table A.1. One of these lines is heavily blended with the $J=15-14$ line of C₃S. The observed velocities are systematically shifted by 0.15 km s^{-1} with respect the velocity of CCO, C₃O, HCCO, and HC₃O. This is a result of the low accuracy, 40-100 kHz, of the laboratory measurements for this transition (see Table A.1 and Pickett & Boyd (1978)). We adopted a rotational temperature of 7 K and derived a column density of $(1.1 \pm 0.1) \times 10^{12} \text{ cm}^{-2}$.

Appendix B.2: HCCO

We note that HCCO has an electronic ground state $^2A''$ and its rotational transitions with $K_a=0$ have been observed in the laboratory by different authors (Endo & Hirota , 1987; Ohshima & Endo , 1993; Chantzos et al. , 2019). The dipole moment of the molecule has been estimated through ab initio calculations to be $\mu_a=1.59 \text{ D}$, with a small component along the b axis of the molecule (Szalay et al. , 1996; Müller et al., 2005). Predictions for the transitions of this molecule are provided in the CDMS catalogue (Müller et al., 2005) and have been implemented in MADEX. The molecule has been detected towards several cold dark clouds by Agúndez et al. (2015). The $N = 2 - 1$ transition has been observed with the QUIJOTE line survey. The six fine and hyperfine components are shown in Fig. B.2. The derived line parameters are given in Table A.1. Two transitions of HCCO, the $N = 4 - 3$ and $N = 5 - 4$, have also been observed in our 3mm data. The four strongest hyperfine components of the $N = 4 - 3$ are detected at the 3σ level and their parameters are given in Table A.1. For the $N = 5 - 4$ transition, only upper limits of 11 mK (3σ) are obtained. Adopting the rotational temperature of CCO (7 K), and a source of uniform brightness with a diameter of $80''$ (Fossé et al., 2001), we derived a column density of $(7.7 \pm 0.7) \times 10^{11} \text{ cm}^{-2}$. The synthetic spectrum for the $N = 2 - 1$ transition is shown in red in Fig. B.2 and matches the observed lines rather well. The predicted intensities for the $N = 4 - 3$ lines are in agreement with the derived parameters for the four strongest hyperfine components of this transition.

Appendix B.3: HC₅O and HC₇O

It is important to note that HC₅O is a linear molecule with a $^2\Pi_r$ state and its $^2\Pi_{1/2}$ rotational spectrum has been observed in the laboratory by Mohamed et al. (2005), who also provided an estimate of the dipole moment of 2.16 D from ab initio calculations. The molecule has been detected in TMC-1 by McGuire et al. (2017) through the detection of the two Λ -components, each one splitted in two hyperfine components, of the $J=17/2-15/2$ rotational transition at 21.85 GHz. In Fig. B.3 we report the two Λ -components of seven rotational transitions from $J=25/2-23/2$ up to $J=37/2-35/2$. The signal-to-noise ratio for each individual line is larger than 30. Line parameters for the observed lines are given in Table A.1. The derived velocities of the observed tran-

sitions are $\sim 5.75 \text{ km s}^{-1}$, that is similar to those of the lines of C₃O. We adopted a rotational temperature of 10 K and derived a column density for HC₅O of $(1.4 \pm 0.2) \times 10^{12} \text{ cm}^{-2}$. This value is in good agreement with the column density of $1.7 \times 10^{12} \text{ cm}^{-2}$ derived by McGuire et al. (2017).

We note that HC₇O also has a $^2\Pi_r$ ground electronic state and its rotational spectrum has also been derived from Mohamed et al. (2005). The transitions falling within the QUIJOTE line survey have large J numbers and energies above 20 K. This molecule was reported as detected through stacking techniques by Cordiner et al. (2017). These authors assume a rotational temperature of 6 K and obtain a column density of $(7.8 \pm 0.9) \times 10^{11} \text{ cm}^{-2}$. Using these values, we predict an antenna temperature of 0.5 mK for the $J=57/2-55/2$ e and f Λ -doubling components (31.275 GHz). No other lines could be detected within the sensitivity of the QUIJOTE line survey for this rotational temperature. However, we have explored all the lines up to 40 GHz and found several lines of HC₇O up to the $J=69/2-67/2$. They are shown in Fig. B.4. Although some of the lines are blended with other lines or with negative features resulting from the folding of the frequency switching data, the detection of HC₇O is now secure and based on the detection of several individual lines. The observed velocities range from between 5.5 and 6 km s⁻¹, which is probably due to the limited signal-to-noise ratio for the weak emission of this species, and to the large extrapolation in quantum numbers compared with the laboratory data ($v_{max}=19.2 \text{ GHz}$, $J_{max}=35/2$).

A rotational diagram indicates that the rotational temperature of HC₇O could be close to 10 K, rather than the 6 K previously assumed (Cordiner et al. , 2017). Using a model fitting to the observed line profiles (Cernicharo et al., 2021d) with a rotational temperature of 10 K, we derived a column density of $(6.5 \pm 0.5) \times 10^{11} \text{ cm}^{-2}$, which is in reasonable agreement with the value of Cordiner et al. (2017). Although our data cannot support a rotational temperature as low as the value adopted by Cordiner et al. (2017), the effect on the derived column density is moderate. This effect has been discussed in detail in the analysis of the column density of HCS⁺ and HC₃S⁺ (Cernicharo et al., 2021f). The HC₅O/HC₇O abundance ratio is 2.2 ± 0.3 .

We searched for HC₄O and HC₆O without success. The derived upper limits are given in Table 1.

Appendix C: C_nO species

Appendix C.1: Dicarbon Monoxide, CCO

This molecule has a $^3\Sigma^-$ ground electronic state and its microwave and millimetre wave spectra are well-known (Yamada et al. , 1985; Ohshima et al. , 1995). We note that CCO was detected in TMC-1 by Ohishi et al. (1991). The laboratory data cover frequencies up to 184.8 GHz and $J_{max}=9$, which guarantees excellent frequency predictions in the frequency domain of our line survey. A dipole moment of 1.305 D was derived through ab initio calculations by Thomson & Wishart (1973). The lines observed with the Yebes 40m and IRAM 30m radio telescopes are shown in Fig. B.5, and the derived line parameters for all lines are given in Table A.1. A rotational diagram assuming a source of uniform brightness temperature and $80''$ in diameter (Fossé et al., 2001) provides a rotational temperature of $7.0 \pm 1.5 \text{ K}$ and a column density of $(7.5 \pm 0.3) \times 10^{11} \text{ cm}^{-2}$. This value is in good agreement with that obtained by Ohishi et al. (1991), and it is slightly smaller than the one derived by Cernicharo et al. (2020a) who assumed an uniform rotational temperature of 10 K and did not consider the 3mm lines. The effect of the adopted rotational

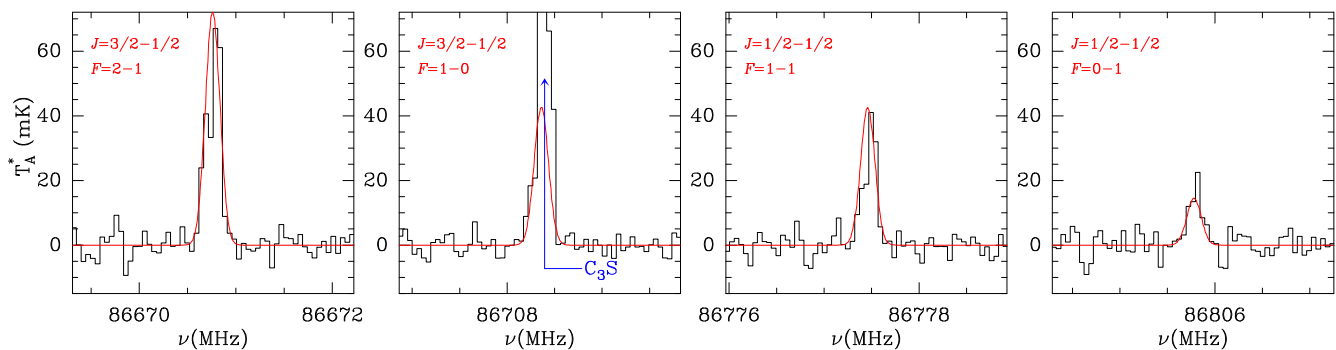


Fig. B.1. Observed lines of the $1_{01} - 0_{00}$ transition of HCO in TMC-1. The abscissa corresponds to the rest frequency of the lines. The v_{LSR} , linewidth, and integrated intensity of each line are provided in Table A.1. The ordinate is the antenna temperature, corrected for atmospheric and telescope losses, in milli Kelvin. The noise of this spectrum is 3.7 mK. The quantum numbers for each transition are indicated. The red line shows the computed synthetic spectrum for this species (see Appendix B.1).

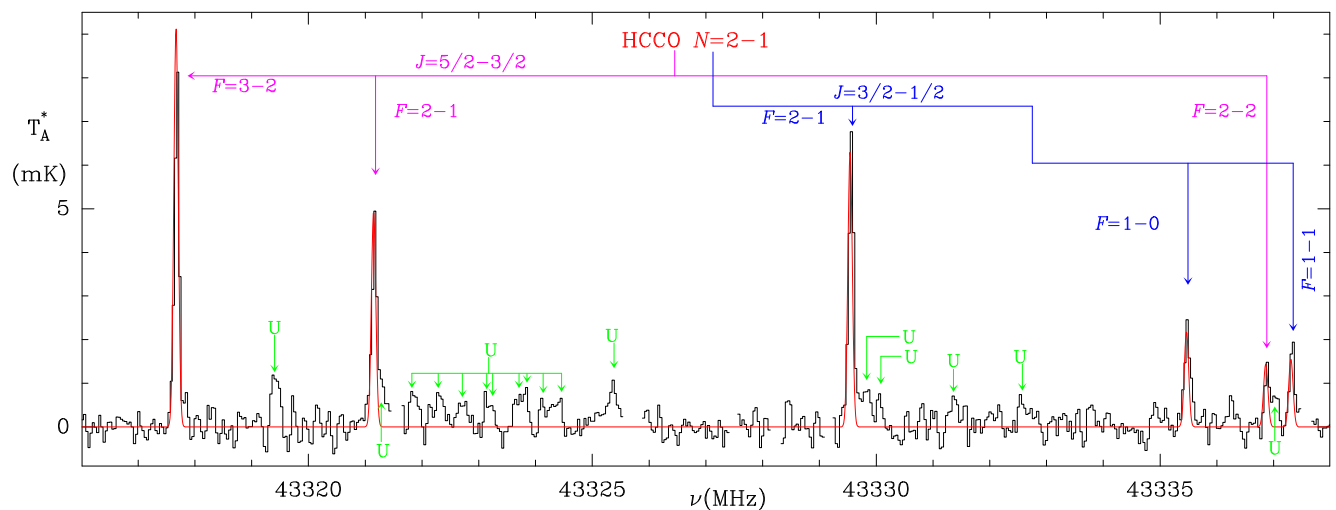


Fig. B.2. Observed lines of the $2_{02} - 1_{01}$ transition of HCCO in TMC-1. The abscissa corresponds to the rest frequency of the lines. The v_{LSR} , linewidth, and integrated intensity of each line are given in Table A.1. The ordinate is the antenna temperature, corrected for atmospheric and telescope losses, in milli Kelvin. The noise of this spectrum is 0.22 mK. The quantum numbers for each transition are indicated. The hyperfine components of the fine structure transitions $J=5/2-3/2$ and $J=3/2-1/2$ are indicated in violet and blue, respectively. The red line shows the computed synthetic spectrum for this species (see Appendix B.2). Blank channels correspond to negative features produced in the folding of the frequency switching data.

temperature on the column density is much more critical for this $^3\Sigma^-$ molecule than for a linear species of a similar rotational constant. This is due to the large energy difference between the levels $J = N - 1$, N , and $N + 1$, and the possible propensity rules for collisions between these levels. The comparison of the observed intensities at 3 and 7mm suggest that at 3mm ($N = 4$) the excitation temperature is below 6 K, while at low frequency it could be close to the kinetic temperature of 10 K.

In order to evaluate the possible excitation effects, we used the MADEX code to perform a large velocity gradient calculation (LVG; MADEX follows the formalism described by Goldreich & Kwan (1974)). For this purpose, we adopted the collisional rates of OCS (Green & Chapman, 1978) and the infinite-order-sudden approximation for a $^3\Sigma$ molecule (Alexander & Dagdigan, 1983; Corey & McCourt, 1983; Fuente et al., 1990). For a volume density of $4 \times 10^4 \text{ cm}^{-3}$, the excitation temperatures obtained using this approach are ~ 10 K for the lines observed at low frequency (QUIJOTE data). However, the excitation temperature decreases very fast to 6.5 K for $N=4$ and to ~ 5.5 K for $N=5$. We have explored the effect of $n(\text{H}_2)$ on the excitation temperatures of CCO. For $n(\text{H}_2) \geq 9 \times 10^3 \text{ cm}^{-3}$, the $N=1$ and 2 lines have an excitation temperature close to T_K . However, the lines

associated with the levels with $N=4$ show a sharp dependence of T_{exc} with density. The best fit to the observations is obtained for $n(\text{H}_2) = 10^4 \text{ cm}^{-3}$ and $N(\text{CCO}) = 7.5 \times 10^{11} \text{ cm}^{-2}$, that is, the value derived from the rotational diagram. For this density, the excitation temperature of the $N=5$ lines decreases to 4-5 K.

The synthetic spectrum computed with the parameters resulting from the best fit is shown in Fig. B.5. The match between the observations and the model is rather good despite the uncertainties on the adopted collisional rates, which also affect the derived volume density. Collisional rates for CCO are needed in order to derive more accurate physical conditions from its rotational transitions.

Appendix C.2: Oxopropadienylidene, CCCO

There is an extensive literature on laboratory experiments concerning the centimetre, millimetre, and sub-millimetre spectroscopy of oxopropadienylidene (Brown et al., 1983; Tang et al., 1985; Klebsch et al., 1985; Bogey et al., 1986; Bizzocchi et al., 2008). The data cover frequencies up to 740 GHz and $J_{max} = 77$. The molecule has a dipole moment of 2.39 D (Brown et al., 1983). This molecule has been detected in the interstel-

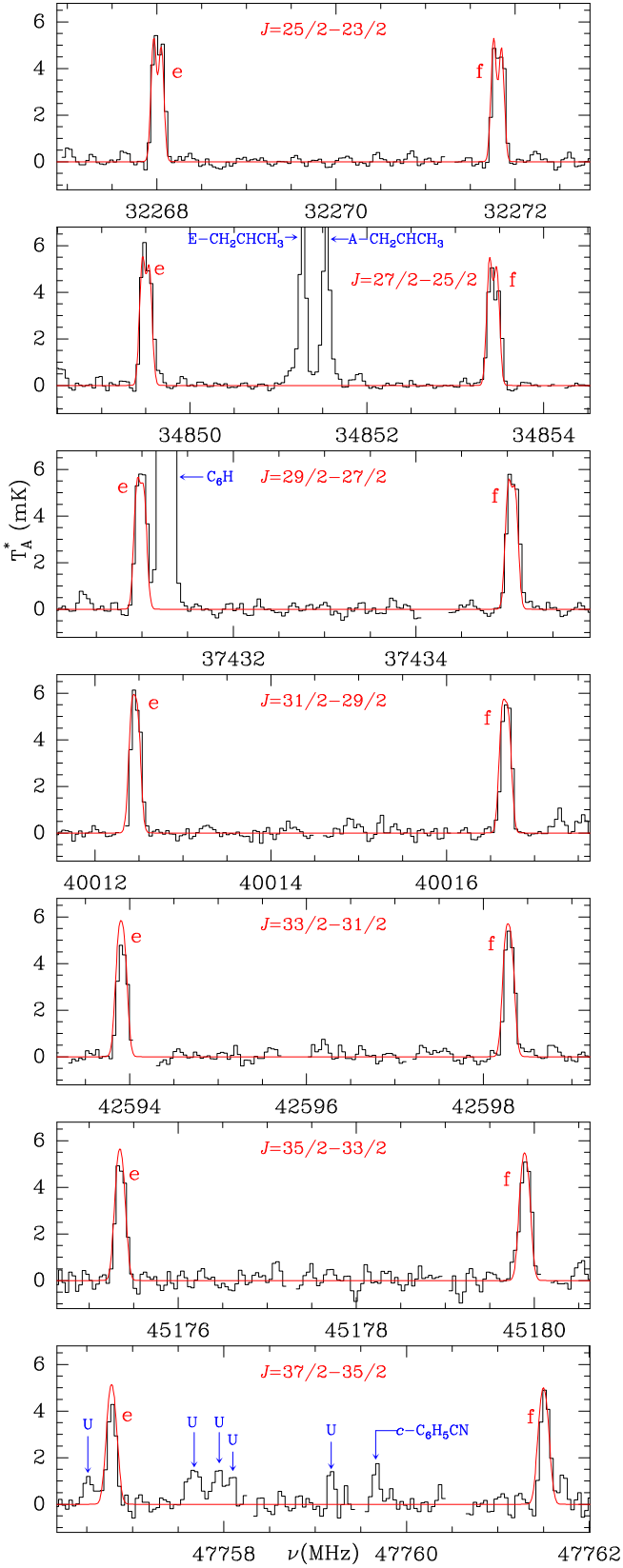


Fig. B.3. Observed lines of HC_5O in TMC-1. The abscissa corresponds to the rest frequency of the lines. The v_{LSR} , linewidth, and integrated intensity of each line are given in Table A.1. The ordinate is the antenna temperature, corrected for atmospheric and telescope losses, in milli Kelvin. The quantum numbers for each transition are indicated. The red line shows the computed synthetic spectrum for this species (see Appendix B.3). Blank channels correspond to negative features produced in the folding of the frequency switching data.

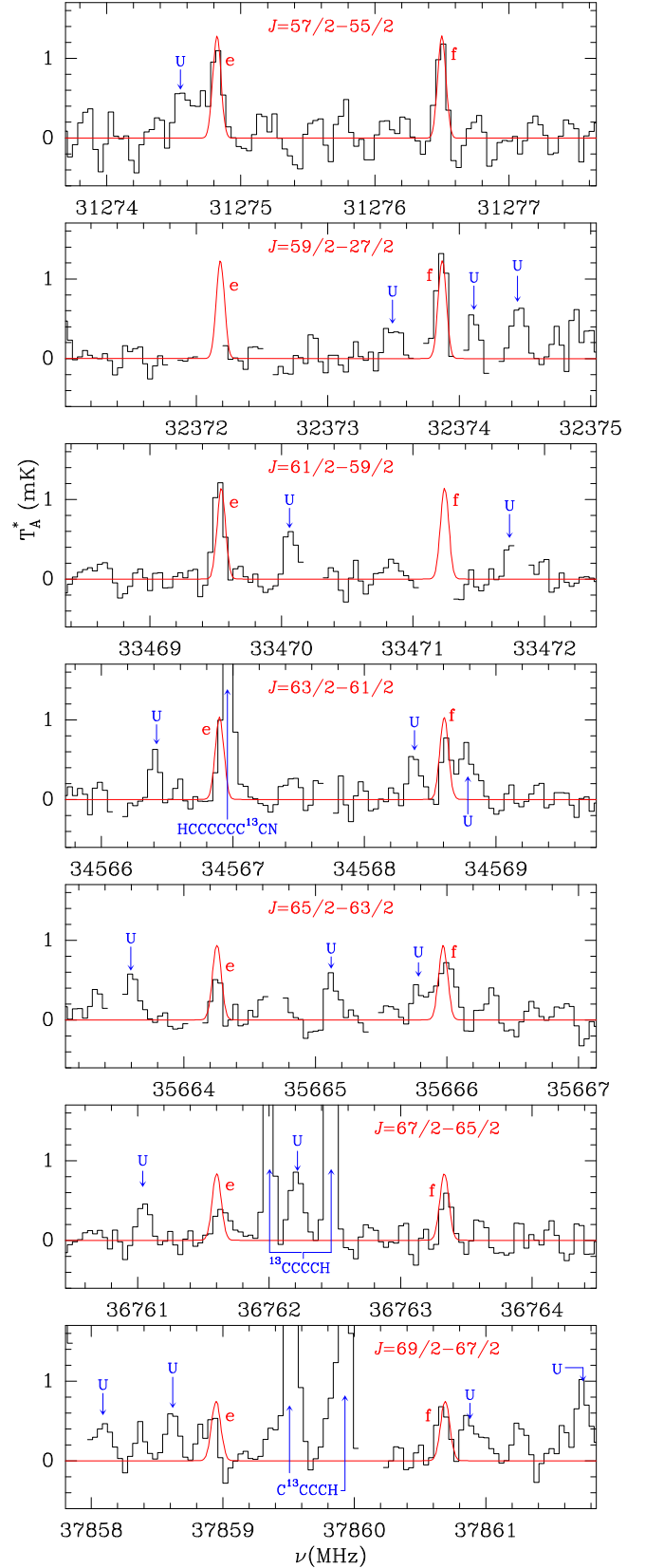


Fig. B.4. Observed lines of HC_7O in TMC-1. The abscissa corresponds to the rest frequency of the lines. The v_{LSR} , linewidth, and integrated intensity of each line are given in Table A.1. The ordinate is the antenna temperature, corrected for atmospheric and telescope losses, in milli Kelvin. The quantum numbers for each transition are indicated. The red line shows the computed synthetic spectrum for this species (see Appendix B.3). Blank channels correspond to negative features produced in the folding of the frequency switching data.

lar and circumstellar media (Matthews et al., 1984; Brown et al., 1985; Tenenbaum et al., 2006). The protonated form of this species, HCCCO⁺, has been recently detected in TMC-1 (Cernicharo et al., 2020a). A study of CCO and CCCO in low-mass star-forming regions has been recently made by Urso et al. (2019).

The observed lines with the Yebes and IRAM radio telescopes are shown in Fig. C.1. The derived line parameters are given in Table A.1. Assuming a source of 80'' in diameter with a uniform brightness temperature, we obtain a rotational temperature of 7 ± 1 K and a column density of $(1.2\pm 0.2)\times 10^{12}$ cm⁻². This value is in good agreement with that reported by Matthews et al. (1984), Brown et al. (1985), and Cernicharo et al. (2020a). The synthetic spectrum computed for these values of the rotational temperature and the column density is shown by the red lines in Fig. C.1. The agreement between the model and observations is excellent. In order to check the assumption of a uniform rotational temperature for all rotational levels of CCCO, which could be the main source error in the determination of the column density (Cernicharo et al., 2021b), we performed large velocity gradient calculations adopting the collisional rates of HC₃N (Faure et al., 2016) for CCCO. Adopting a density of 4×10^4 cm⁻³ (Cernicharo & Guélin, 1987; Fossé et al., 2001), we obtain an excitation temperature of ~ 10 K for all levels below $J \leq 5$, and a continuous decrease in T_{exc} with increasing J , reaching a value of ~ 6 K for $J = 11$. Hence, the derived rotational temperature is strongly determined by the transitions with high- J levels observed with the IRAM 30m radio telescope.

Appendix C.3: C₄O and C₆O

We note that C₄O and C₆O were observed in the laboratory by Ohshima et al. (1995). Both have a $^3\Sigma^-$ ground electronic state. These molecules have been implemented in MADEX and we searched for their strongest transitions within the QUIJOTE line survey. None of their lines are detected. Assuming a rotational temperature identical to that of C₅O ($T_{rot}=10$ K), we derived 3σ upper limits to their column density of 9.0×10^{10} and 1.1×10^{11} cm⁻², respectively.

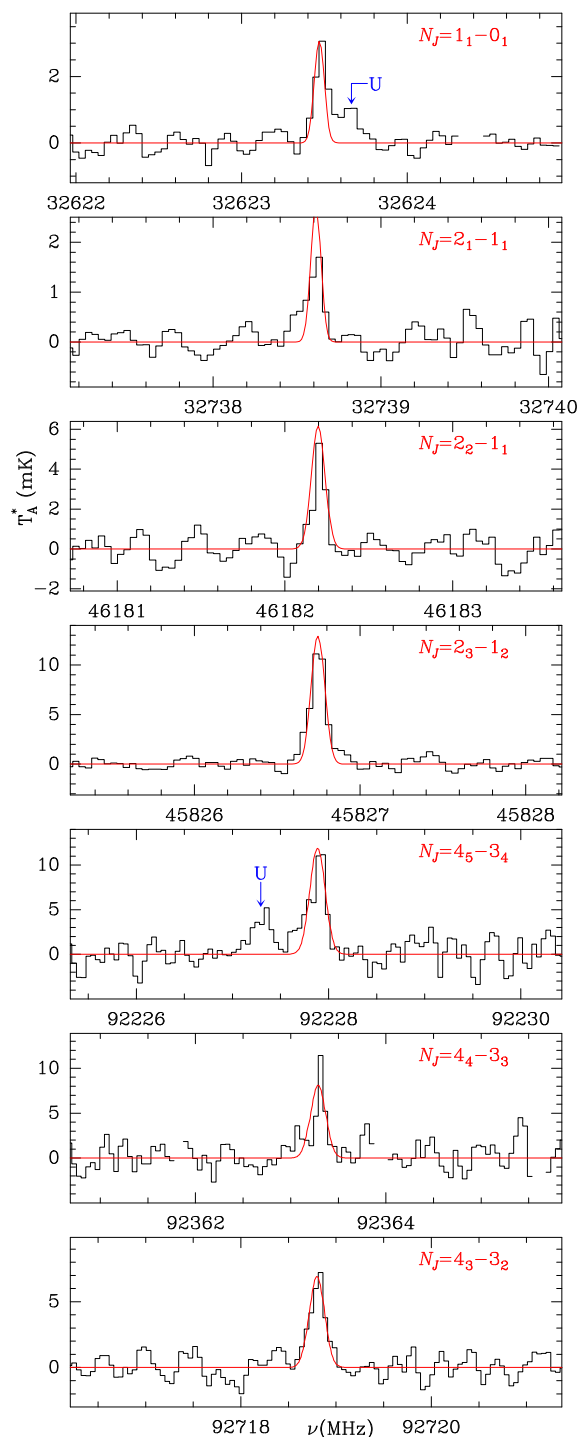


Fig. B.5. Observed transitions of CCO in our line survey towards TMC-1. The abscissa corresponds to the rest frequency of the lines. The v_{LSR} , linewidth, and integrated intensity of each line are given in Table A.1. The ordinate is the antenna temperature, corrected for atmospheric and telescope losses, in milli Kelvin. The quantum numbers for each transition are indicated in the upper right corner of the corresponding panel. The red line shows the computed synthetic spectrum for this species (see Appendix C.1). Blank channels correspond to frequencies affected by negative features produced in the folding of the frequency switching data.

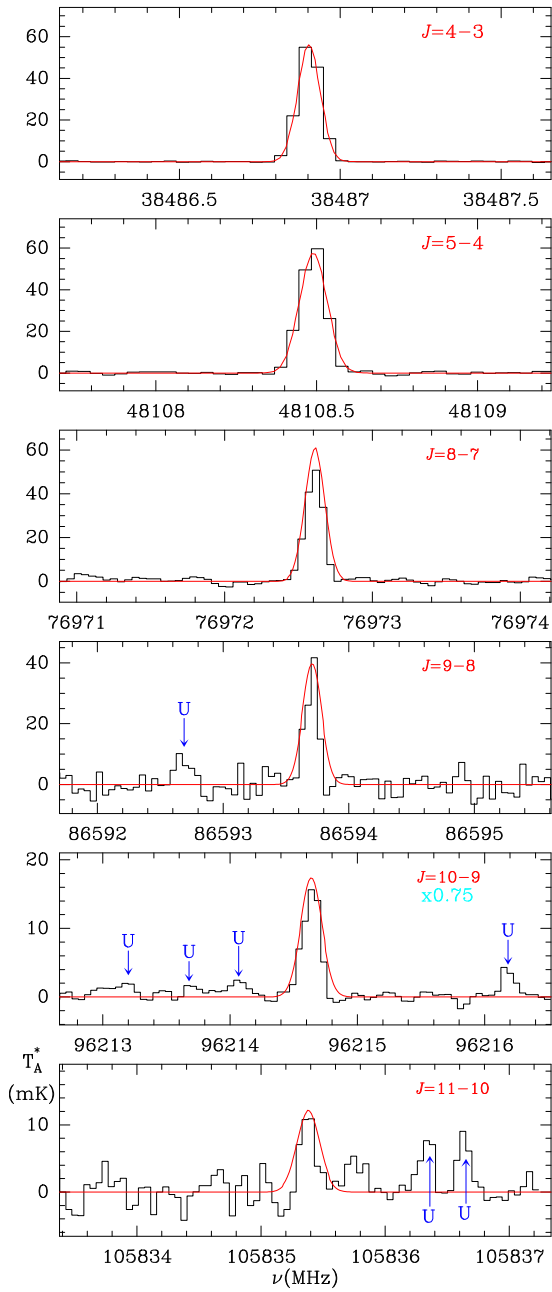


Fig. C.1. Observed transitions of C_3O in TMC-1. The abscissa corresponds to the rest frequency of the lines. Their v_{LSR} , linewidth, and integrated intensity of each line are given in Table A.1. The ordinate is the antenna temperature, corrected for atmospheric and telescope losses, in milli Kelvin. The quantum numbers for each transition are indicated in the upper right corner of the corresponding panel. The red line shows the computed synthetic spectrum for this species (see Appendix C.2).